

Measurement of seismometer misorientation based on *P*-wave polarization: application to permanent seismic network in South Korea

Young Oh Son, Min-Seong Seo, and YoungHee Kim*

School of Earth and Environmental Sciences, Seoul National University, Seoul 08826, Republic of Korea

ABSTRACT: Reliable information on the horizontal orientation of a seismometer is crucial to seismological research utilizing three-component seismograms. In this study, we provide misorientation angles of broadband seismometers in three permanent networks in South Korea from 2003 to 2021 by using two methods, denoted as P_{PCA} and P_{minT} , both utilizing *P*-wave polarization characteristics. Our estimates show that 36% of the sensors have been aligned within 5° from the geographic north during their operation periods, while 40% of the sensors have been rotated by more than 10° at least once. The estimates are highly consistent for both methods, with 95% of the total showing uncertainty less than 10°. Moreover, we identified a significant number of temporal changes in misorientation by taking automatic change point detection and visual inspection. The procedure described here and misorientation angles can be useful reference for seismic data preprocessing for research utilizing horizontal-component seismograms for earthquake sciences.

Key words: misorientation, *P*-wave polarization, principal component analysis, minimization of transverse *P*-wave energy, change point detection

Manuscript received June 13, 2021; Manuscript accepted September 2, 2021

1. INTRODUCTION

The assessment of the quality of seismic data as preprocessing step is prerequisite for seismological research, and all the efforts aim to better constrain subsurface seismic structure of the Earth, earthquake source properties, characteristics of seismic and man-made noise, etc. If the seismic instrument is miscalibrated or improperly installed, the measures will be inaccurate; furthermore, if no correction is applied, this will generate inaccurate data and thus degrade the quality of research results. The misalignment of the seismometer leads to inaccurate horizontal components. Ekström and Nettles (2018) examined the sensor orientation of the 1857 USArray stations operated during 2006–2015 and

reported that the orientation errors were greater than 3° for 12% of the entire fleet of stations. Several other studies that assessed orientation angles of seismometers (Laske et al., 1994; Niu and Li, 2011; Rueda and Mezcua, 2015; Wang et al., 2016; Ojo et al., 2019; Braunmiller et al., 2020) reported that a significant proportion of their sensors was misaligned, indicating that sensor misorientation is a widespread issue. Even slight misalignment in the horizontal components can be critical to research utilizing three-component data such as shear wave splitting analysis (e.g., Liu and Gao, 2013), moment tensor inversion (e.g., Zahradník and Custódio, 2012), receiver function analysis (e.g., Zhu et al., 2019), and earthquake early warning (e.g., Eisermann et al., 2015).

In South Korea, there are three permanent seismic networks: 1) the KG network operated by the Korea Institute of Geoscience and Mineral Resources (KIGAM), 2) the KS network operated by the Korea Meteorological Administration (KMA), and 3) the KN network operated by the Korea Hydro and Nuclear Power (KHNP) (Lim and Kim, 2020). These permanent stations provide valuable seismic waveform data for various studies aiming to elucidate earthquake properties and seismic structure of the Korean Peninsula (Kang and Baag, 2004; Kim et al., 2010; Kim et al., 2016; Kim et al., 2017; Kim et al., 2018; Woo et al., 2019; Lim et al., 2020). The number of seismic stations has increased

*Corresponding author:

YoungHee Kim
School of Earth and Environmental Sciences, Seoul National University,
1 Gwanak-ro, Gwanak-gu, Seoul 08826, Republic of Korea
Tel: +82-2-880-6735, E-mail: younghkim@snu.ac.kr

Electronic supplementary material

The online version of this article (<https://doi.org/10.1007/s12303-021-0031-5>) contains supplementary material, which is available to authorized users.

continuously since the modern KMA seismograph network operation started in 1978. In light of the recent M_L 5.8 Gyeongju earthquake in 2016 and the M_L 5.4 Pohang earthquake in 2017, the importance of seismic observation in South Korea has gained significant public attention, leading to the deployment of a greater number of seismic stations. Despite this latest expansion of seismic stations, the quality of seismic signals and potential installation errors have not been systemically evaluated. We here aim to enhance the quality of the seismic data by detecting potential misorientation issues and also by providing the misorientation angles for the stations that we examined.

In this study, we used methods based on P -wave polarization to accurately measure the misorientation angles of 150 permanent broadband stations. Although there are several notable studies on the misorientation angles of seismic stations in South Korea (Shin et al., 2009; Lee and Rhie, 2015; Lee and Sheen, 2015), these studies are limited to only small sets of stations that are valid for the period of maximum 21 months. Recent work by Lim et al. (2018) proposed the method based on teleseismic receiver functions and provided orientation angles for 52 broadband stations for the maximum of 10 years. In this study, we attempted to use seismic records for the longest duration possible (maximum 17 years), including more recent data that were not included in previous studies. We also developed a rapid and robust method capable of detecting temporal variations in misorientation angles for each seismic station, which can be compared against the sensor log provided by the seismic networks.

2. DATA

We calculated the misorientation of the KG, KS, and KN networks, using waveforms for earthquakes recorded from three-component broadband seismometers at each network. Since 1994, KIGAM and KMA have steadily expanded the number of KG and KS broadband seismometers, reaching a total of 29 and 96 for the ones in operation up to now, respectively, according to the KMA database. KHNP currently operates 13 broadband seismic stations to evaluate the seismic stability of nuclear power plant sites since 1999, equipped with sensors and recorders replaced in 2017 (Park et al., 2018). The KG and KS networks provide the data in both BH and HH channels with sampling rates of 20 Hz and 100 Hz, respectively. Meanwhile, the KN network provides the data in HH channel only with sampling rates of 100 Hz. The number of stations with BH and HH channels in each network used in this study is presented in Table 1. Figure 1 illustrates the geographic distribution of the permanent networks (KG, KS, and KN).

To obtain a clear and consistent P -wave signal, we set criteria

Table 1. The number of stations in each network for BH and HH channels used in this study

	KG	KS	KN
BH	26 (12) ^(a)	74 (50)	0 (0)
HH	26 (12)	110 (81)	13 (0)

^(a)The number in each bracket indicates the number of borehole stations containing corresponding channel in each network.

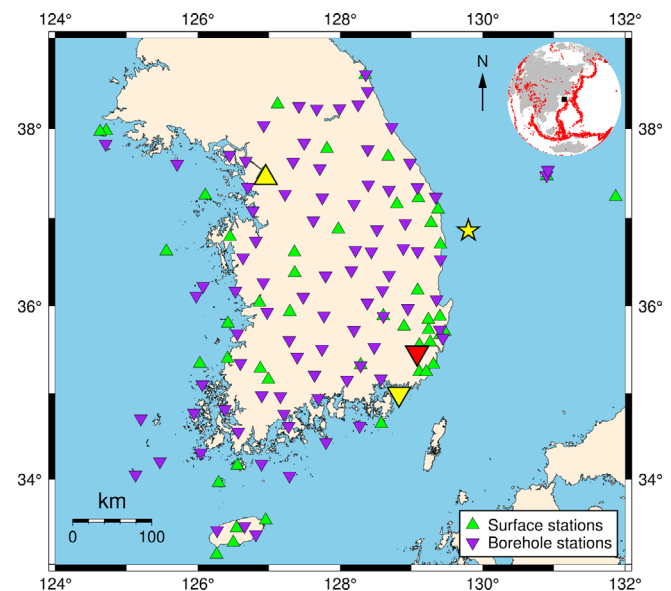


Fig. 1. The map of stations and earthquakes used in this study. Stations with surface seismometers and borehole seismometers are marked as green triangles and purple inverted triangles, respectively. The locations of earthquakes are marked as red dots in the inset, with distances ranging within 90° from the center point (36.5°N, 128°E), marked as a black square. Red inverted triangle marks the location of YSB station, and yellow triangle and inverted triangle indicate SNU station and GDD station, respectively. Yellow star represents the epicenter of 21 April 2019 Uljin earthquake.

for moment magnitude (M_W) and the epicentral distance of earthquakes used in the misorientation calculation. We selected earthquakes with a M_W value greater than 6.0 and with an epicentral distance ranging from 0° to 90° with respect to a location of 36.5°N, 128°E for the KG and KS networks. For the KN network, we lowered the M_W threshold to 5.5 to increase the sample size, given that the operational period is much shorter than that of other networks. The inset of Figure 1 shows the distribution of 6736 earthquakes used in this study. We removed the mean and trend of waveforms, and then applied tapering and zero-phase band-pass filtering within the frequency range of 0.02–0.2 Hz. We selected the passband referring to the previous researches on seismometer misorientation based on the P -wave polarization analysis (Niu and Li, 2011; Wang et al., 2016; Ojo et al., 2019; Zeng et al., 2020). For the HH channel of KG, KS, and KN, we downsampled the data points from 100 Hz to 20 Hz for efficient computation.

3. METHOD

There are several methods that can constrain sensor misorientation from seismic waveform records. Previous studies used the body wave polarization measurement (Shin et al., 2009; Niu and Li, 2011; Lee and Sheen, 2015; Scholz et al., 2017; Wang et al., 2016; Ensing and van Wijk, 2018; Ojo et al., 2019; Braunmiller et al., 2020; Xu et al., 2020; Zhu et al., 2020; Büyükakpınar et al., 2021; Zeng et al., 2020), surface wave polarization measurement (Stachnik et al., 2012; Rueda and Mezcua, 2015; Scholz et al., 2017; Doran and Laske, 2017; Ojo et al., 2019; Xu et al., 2020; Zhu et al., 2020; Büyükakpınar et al., 2021), comparative analysis of observed and synthetic waveforms (Ekström and Busby, 2008; Ekström and Nettles, 2018; Braunmiller et al., 2020), ambient noise cross-correlation (Zha et al., 2013; Lee and Rhie, 2015; Xu et al., 2018; Ensing and van Wijk, 2018; Zeng et al., 2020), and receiver function analysis (Lim et al., 2018; Zheng et al., 2020). In this study, we explored two methods based on *P*-wave polarization for estimating the misorientation of seismometers considering computational efficiency and relative ease in implementation for rapid assessment of the station quality.

The first method directly measures the dominant particle motion of the *P* wave via principal component analysis (PCA) (Pearson, 1901), which we denote as the P_{PCA} method. The second method is based on a property of the *P* wave, which is rarely observed on the transverse component if the seismometer is correctly oriented: the P_{minT} method. Details on the two methods are described in subsequent two sections.

Before detailing the methods in greater depth, we briefly define the misorientation angle in terms of back azimuth as Figure 2 illustrates. Figure 2 shows a schematic of misoriented

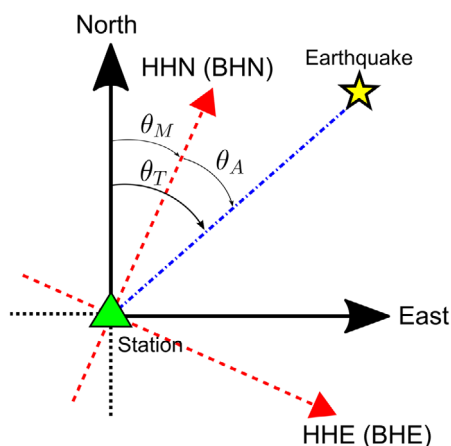


Fig. 2. A schematic plot describing the relationship between the theoretical back azimuth (θ_T) of an earthquake (star) and the apparent back azimuth (θ_A) of the same earthquake. The station is assumed to be located at the origin. The misorientation angle (θ_M) is defined clockwise from the geographic north to the north component of the horizontal sensors.

horizontal components of a sensor with respect to the geographic north and east. Let us assume that the N-S component of the sensor is rotated from the geographic north by an angle θ_M . The theoretical back azimuth of an earthquake is defined by an angle θ_T . Under this geometrical scheme, the apparent back azimuth of an earthquake relative to the station is defined as angle θ_A . The method used in this study estimates the apparent back azimuth θ_A of a selected earthquake and subtracts it from the theoretical azimuth θ_T to obtain the misorientation angle: $\theta_M = \theta_T - \theta_A$. If the seismometer is properly oriented, the apparent back azimuth and the theoretical back azimuth will be equal.

3.1. Measurement of the *P*-wave Particle Motion from the P_{PCA} Method

The P_{PCA} method estimates the back azimuth of an earthquake by analyzing the dominant particle motion of the *P* wave recorded at a particular station. Shin et al. (2009) tested two methods for polarization analysis: one using all three components of the seismometer and the other using only the horizontal components. They concluded that the former provides greater stability. We thus used the three-component polarization to estimate the apparent back azimuths of each event that passed the quality criteria, as will be detailed in Section 4.1.

We applied PCA to estimate the *P*-wave polarization following the scheme by Jurkevics (1988). First, we chose the time window containing the *P*-wave signal of an earthquake by determining the optimal pair of time window lengths before and after theoretical *P*-wave arrival, which is calculated using global velocity model IASP91 (Kennett and Engdahl, 1991). The detail of this procedure is presented in Section 3.4. Next, we calculated the covariance matrix **S** from the data matrix

$$\mathbf{X} = [\mathbf{z}, \mathbf{n}, \mathbf{e}], \quad (1)$$

where **z**, **n**, and **e** stand for the column vectors of *N* data points in the predetermined time window for vertical, N-S, and E-W components, respectively. The covariance matrix **S** of **X** was calculated as

$$\mathbf{S} = \frac{\mathbf{X}^T \mathbf{X}}{N} = \frac{1}{N} \begin{bmatrix} \mathbf{z}^T \mathbf{z} & \mathbf{z}^T \mathbf{n} & \mathbf{z}^T \mathbf{e} \\ \mathbf{n}^T \mathbf{z} & \mathbf{n}^T \mathbf{n} & \mathbf{n}^T \mathbf{e} \\ \mathbf{e}^T \mathbf{z} & \mathbf{e}^T \mathbf{n} & \mathbf{e}^T \mathbf{e} \end{bmatrix}. \quad (2)$$

We then solved the eigenproblem

$$(\mathbf{S} - \lambda^2 \mathbf{I}) \mathbf{u} = \mathbf{0}, \quad (3)$$

to find the set of eigenvalues ($\lambda_1, \lambda_2, \lambda_3$) such that $\lambda_1 \geq \lambda_2 \geq \lambda_3$ and the corresponding set of eigenvectors (**u**₁, **u**₂, **u**₃). Since the noise in each component was uncorrelated, the covariance

matrix \mathbf{S} was usually well-conditioned and the eigenproblem could be solved robustly and efficiently using standard numerical libraries. We used the linear algebra library implemented in NumPy to solve the eigenproblem (Harris et al., 2020). As a result, we obtained three orthogonal unit eigenvectors and three corresponding eigenvalues. Then, the apparent back azimuth of an earthquake can be estimated from the following formula:

$$\theta_A = \tan^{-1} \left[\frac{u_{31} \text{sign}(u_{11})}{u_{21} \text{sign}(u_{11})} \right], \quad (4)$$

where the sign function was introduced to resolve for the 180° ambiguity by taking the positive u_{11} . Here, u_{i1} ($i = 1, 2, 3$) refers to the i^{th} entry of the eigenvector \mathbf{u}_1 that corresponds to the largest eigenvalue λ_1 . Figure 3a schematically describes the basic concept of the P_{PCA} method.

3.2. Minimization of Transverse P -wave Energy: $P_{\min T}$ Method

The $P_{\min T}$ method estimates the back azimuth of an earthquake based on the principle that P wave is radially polarized. In other words, if the seismometer is correctly oriented, the P -wave record must be confined to the radial-vertical plane and minimally observed in the transverse component. Thus, any seismometer misorientation will be manifested as a non-zero P -wave energy value in the transverse component of the recorded seismogram.

The principal idea behind the $P_{\min T}$ method is to estimate an angle δ that minimizes the P -wave transverse energy if the horizontal components are rotated to the radial and transverse components assuming that the back azimuth is δ . Angle δ is then equal to the apparent back azimuth θ_A (shown in Fig. 2). We define the energy of the P wave in the transverse component as

the mean squares of amplitude in the P -wave signal window, which is selected in the same way as the P_{PCA} method. Two candidate rotation angles are used for the minimization of transverse P -wave energy, differing by 180°. To resolve this 180° ambiguity, we computed the zero-lag normalized correlation coefficient (CC) between the radial and vertical components for both candidate angles and selected one with positive CC (Niu et al., 2007; Niu and Li, 2011). Since the particle motion of P wave is parallel to the direction of propagation in principle, we expect the seismic data of radial component and vertical component to have same polarity if the horizontal components are aligned properly, resulting in positive CC. We used *ObsPy*, an open-source Python framework, to rotate the horizontal seismograms and to calculate CC (Beyreuther et al., 2010). Figure 3b schematically describes the grid search scheme to find a rotation angle δ by increasing the rotation angle from 0° to 360° in 1° increments. After finding candidate apparent back azimuths, we repeated the grid search in the range of $[\delta - 0.5^\circ, \delta + 0.5^\circ]$ in 0.1° increments to increase the accuracy of the estimate.

Both methods require a representative value of the misorientation angle and associated uncertainty that is valid for the entire duration of observations for a particular station. We estimated two different values as representative values: the median and trimmed mean (we used the median as it is insensitive to outliers compared to the mean). The median absolute deviation (MAD) was chosen to estimate the uncertainty. Once the median was estimated, we removed outliers outside of the range of $[\text{Median} - 5 \times \text{MAD}, \text{Median} + 5 \times \text{MAD}]$, as done by previous study (Doran and Laske, 2017). Finally, we calculated the mean for the remaining values (the trimmed mean) and its corresponding standard deviation (trimmed SD).

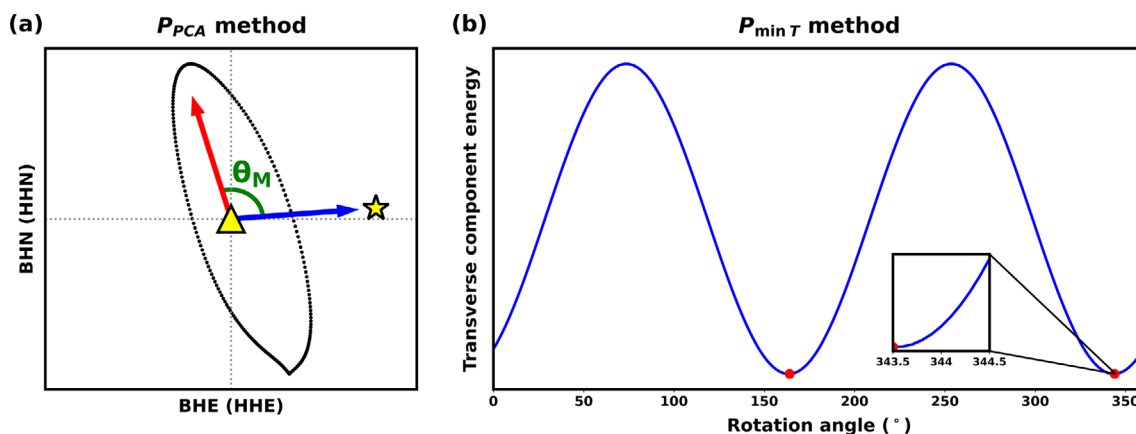


Fig. 3. Schematic diagrams describing the (a) P_{PCA} method and (b) $P_{\min T}$ method. In Figure 3a, black dotted line illustrates the trace of particle motion within the signal window. Yellow triangle and star show the location of station and earthquake, respectively. Red and blue arrows indicate the direction of apparent back azimuth calculated by PCA and theoretical back azimuth, respectively. The angle between these two arrows is the misorientation angle. In Figure 3b, blue line depicts the change of transverse component energy with respect to the rotation angle. Two red dots represent the candidates of apparent back azimuth minimizing the transverse component energy that differ by 180°.

3.3. Monitoring Time-dependent Misorientation

Even at the level of a single seismic station, seismometer misorientation can vary with time due to regular inspection or location change, as reported by several studies (Lee and Sheen, 2015; Lim et al., 2018; Ojo et al., 2019; Braunmiller et al., 2020). Thus, it is necessary to precisely detect such changes in time and measure the misorientation angle at different time intervals.

If seismometer misorientation is clearly visible during regular inspection, we can manually define the period when the sensor was rotated. However, the timing of the rotation can be often subtle and difficult to determine visually; it is also prone to subjective error. To minimize these potential issues, we used a semi-automatic detection method to estimate the period of temporal change regardless of the degree of rotation.

Our proposed approach utilizes the pruned exact linear time (PELT) method (Killick et al., 2012) to detect the temporal change in misorientation. The PELT method is a variant of change point detection algorithm (Aminikhanghahi and Cook, 2017) which selects segments of a given time series with a set of breakpoints where the temporal changes occur. The relevant time series, in our case, is that of the estimated misorientation angles. Therefore, we first applied the PELT method with the appropriate parameters on our estimated time series for the misorientation angles and divided the time series into several candidate segments that define the epochs of sensor misorientation. We used the Python library *ruptures* (Truong et al., 2018), which encompasses a number of change point detection algorithms, to apply the PELT method to our dataset.

We then corrected for the false identification of breakpoints. The PELT method generally yields well-identified segmentation, but the location of breakpoint is susceptible to minor errors. We

developed an interactive scheme to automatically divide the estimated misorientation angle time series for each station based on PELT and manually correct for the potential error. After manual inspection, we obtained the duration of the final time series segments and associated misorientation angles (median and trimmed mean) with corresponding uncertainties (MAD and trimmed SD) for each segment.

3.4. Optimization of Parameters for Quality Control

Several parameters must be calibrated to ensure the quality of misorientation estimates. For the P_{PCA} method, relevant parameters for calibration are the signal-to-noise ratio (SNR), the rectilinearity of the *P*-wave particle motion (recti *P*), and length of the time window to measure the polarization. Here, SNR is defined as

$$\text{SNR} = 10 \log_{10} \frac{S_S}{S_N}, \quad (5)$$

where S_S and S_N are the mean squares of amplitudes of the three-component seismogram in signal and noise windows, respectively. Here we define the noise window as the time window right before the signal window with its length same as that of the signal window. Rectilinearity is defined as

$$\text{recti } P = 1 - \frac{\lambda_2 + \lambda_3}{2\lambda_1}, \quad (6)$$

where λ_i ($i = 1, 2, 3$) was defined in Equation (3) (Jurkevics, 1988). For the $P_{\min T}$ method, the relevant parameters are SNR, CC, and length of the time window to minimize the transverse *P*-wave energy.

We first determined optimal time window length before and after the theoretical *P*-wave arrival (T_p) that constrain the start

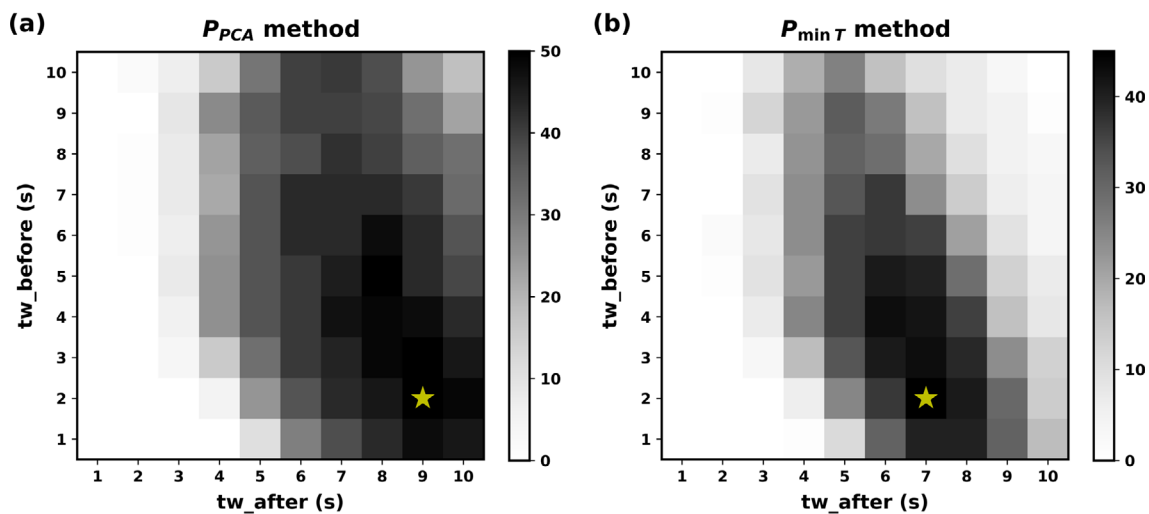


Fig. 4. Heatmap showing the number of reference stations for (a) P_{PCA} method and (b) $P_{\min T}$ method. (a) The number of reference stations reaches its maximum of 50 for signal window ranging from 2 s before to 9 s after T_p , which is marked as yellow star. (b) The number of reference stations reaches its maximum of 45 for signal window ranging from 2 s before to 7 s after T_p , which is marked as yellow star.

and end of the signal window for P_{PCA} method and $P_{\min T}$ method via grid search (Fig. 4). For 100 pairs of the time before T_p and time after T_p both ranging from 1 s to 10 s, we calculated SNR, recti P/CC , and misorientation angle of each event and the median and MAD of the entire misorientation angles of each station. We counted the number of stations with more than 300 events recorded, MAD less than 5° , and the median of recti P or CC over 0.98 and 0.95, respectively (hereafter denoted as reference stations). We selected the time window pair that maximizes the number of reference stations for each method. Then we screened misorientation angles of the entire events against SNR and chose the lower limit of SNR using moving windows each encompassing 10000 events with increasing SNR and overlapping 50% of the adjacent ones (Fig. 5). For each window, we calculated the median of recti P/CC and set the lower limit of SNR, referring to the median of SNR of the window in which the median of recti $P/$

CC first exceeds 0.98/0.95, respectively. After determining the lower limit of SNR, we excluded the events with SNR lower than this threshold or recti P/CC less than 0.98/0.95 and calculated the misorientation angles for the rest of the events.

4. RESULTS AND DISCUSSION

4.1. Optimization of Time Window Length and the Lower Limit of SNR and Recti P/CC

Figures 4a and b show the number of reference stations for each pair of time window length before T_p and after T_p for P_{PCA} method and $P_{\min T}$ method, with yellow stars marking the window pairs that maximize the number of reference stations as 50 and 45, respectively. For P_{PCA} method, the optimal signal window is from 2 s before T_p to 9 s after T_p (Fig. 4a). For $P_{\min T}$

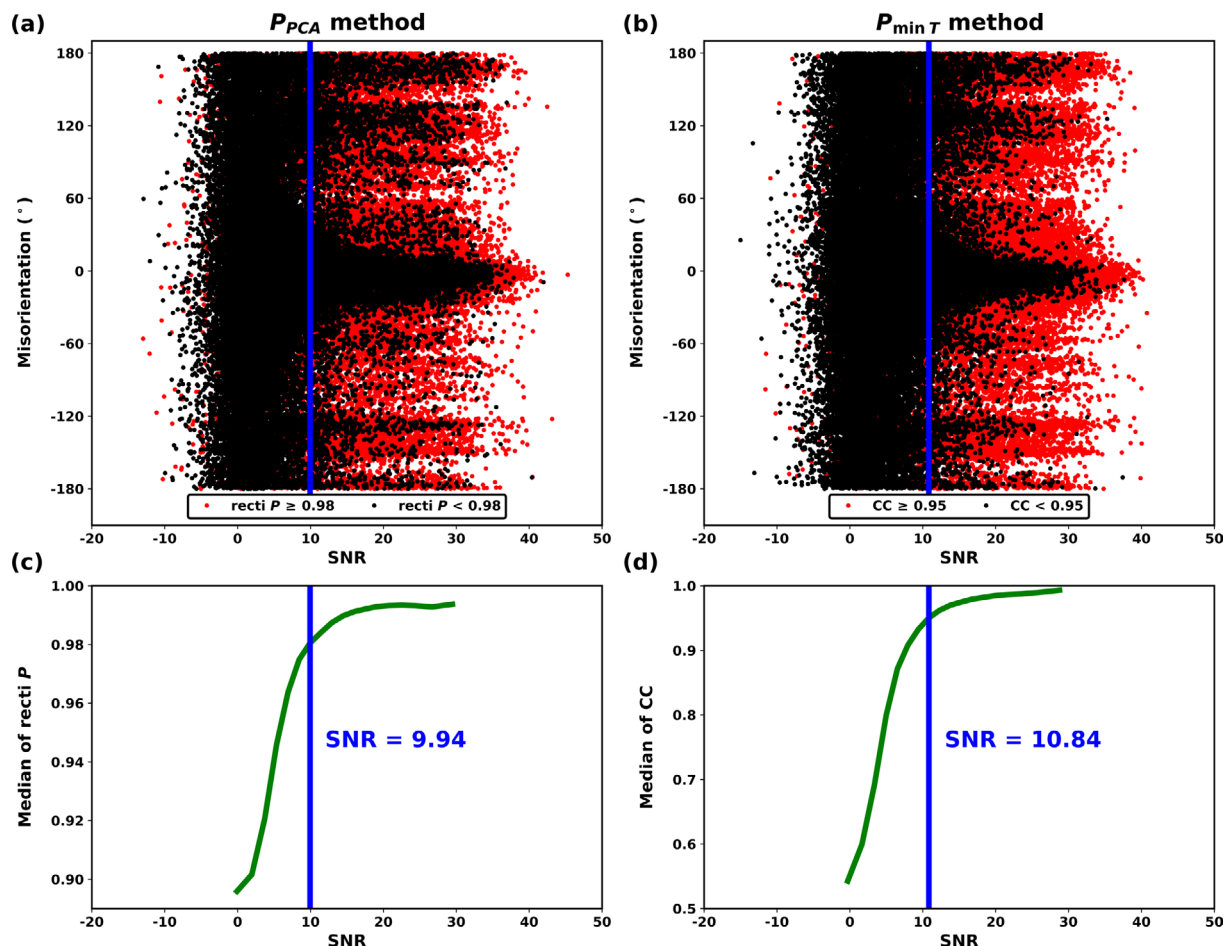


Fig. 5. Distribution of misorientation angles with respect to SNR with the median of recti P and CC calculated by (a, c) P_{PCA} method and (b, d) $P_{\min T}$ method. (a, b) Each dot corresponds to the misorientation angle calculated from a single event, where the red one corresponds to event with (a) recti $P \geq 0.98$ and (b) $CC \geq 0.95$, respectively. Misorientation angles with higher recti P or CC tend to show higher SNR and converge. (c, d) Green curves depict the median of (c) recti P and (d) CC for 50% overlapping moving window with 10000 events, exceeding 0.98 and 0.95 when the median of SNR in the corresponding moving window is over 9.94 and 10.84, respectively. The positions of blue vertical lines indicate SNR thresholds. The misorientation angles range from -180° to 180° since we subtracted 360° from the angles larger than 180° for the ease of plotting.

method, the optimal signal window is from 2 s before T_p to 7 s after T_p (Fig. 4b).

Figures 5a and b show misorientation angles plotted against SNR calculated using the optimal signal window for P_{PCA} method and P_{minT} method, respectively. Red dots indicate the events with recti *P* or CC over 0.98 and 0.95, respectively. These events show higher SNR and misorientation angles with less divergence compared to the others. The median of recti *P*/CC, depicted as a green curve, exceeds 0.98/0.95 when the median of SNR exceeds 9.94/10.84, respectively (Figs. 5c and d). To test the dependence of SNR threshold on the size of moving window, we calculated SNR threshold for various sizes of moving window, and verified that SNR thresholds are close to 10 and 11 regardless of window size for P_{PCA} method and P_{minT} method, respectively. Therefore, we selected SNR threshold of 10 and 11 for P_{PCA} method and P_{minT} method, respectively.

4.2. Compilation of Epoch-dependent Misorientation Angles

After screening the events with low quality, we computed misorientation angles for 26 KG stations, 111 KS stations, and 13 KN stations using the methods of P_{PCA} and P_{minT} . We then applied the change point detection method (see Section 3.3) to define time segments with consistent misorientation angles and with no significant data gap for each station (hereafter denoted as validation period). In most cases, the time segments were identical regardless of method. However, there were several cases where two methods yielded different time segments for the same station. Such cases were particularly prominent for stations associated with small temporal changes in misorientation angle, as the breakpoint detection by PELT is more sensitive to subtle fluctuations in estimated misorientation angles. Therefore, we

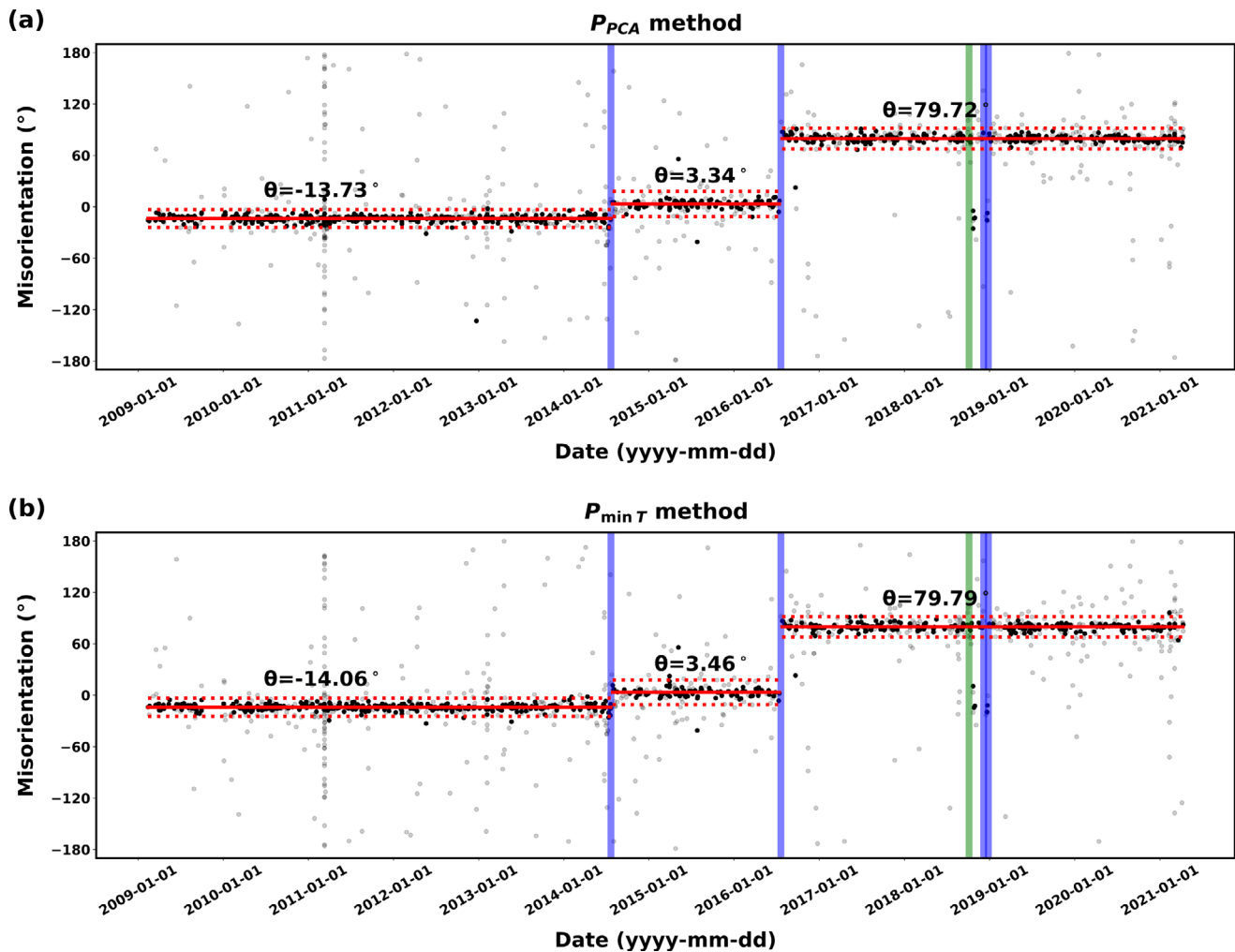


Fig. 6. Time series of misorientation angles with corresponding validation periods of YSB station obtained by (a) P_{PCA} method and (b) P_{minT} method. Red solid line and dotted line indicate the median and $5 \times \text{MAD}$ of each validation period, respectively, with annotation marking the median value. Blue and green lines represent the replacement timing of velocimeter and recorder, respectively. Start timing of the second and third validation periods seem to correlate well with the timing of velocimeter replacement. YSB station is depicted as a red inverted triangle in Figure 1.

assigned validation periods separately for the estimates of two methods. We also extracted the union of these two validation periods and provided a table of combined results so that one can select between the estimates based on two different methods for a common time period. We provide the table of estimated misorientation angles for the KG/KS/KN network in the electronic supplementary material (Table S1).

Figures 6a and b demonstrate the result of validation periods for YSB station in the KG network (Fig. 1), obtained by (a) P_{PCA} method and (b) $P_{min T}$ method with the timing of replacement of the sensor or recorder marked as vertical lines. Each of the black dots corresponds to individual event, where gray dots are the events excluded in the quality control procedure. Blue and green lines indicate the replacement timing of velocimeter and recorder specified in the KIGAM sensor/recorder change log, respectively. In this case, both methods divided the entire time series into 3 distinct validation periods. The start of second and third

validation periods are likely to be related with the replacement of velocimeter.

4.3. Comparison of P_{PCA} and $P_{min T}$ Results

Once the overlapping periods from two methods have been determined, we can directly compare the results obtained by each method. Figure 7 shows a set of diagrams exhibiting the correlation between the results from each method, while also comparing median and mean values calculated by each method. Data from KG, KS, and KN were plotted to compare the robustness of each method (Fig. 7). Figures 7a and b show that the median and mean obtained by both methods are strongly correlated. As expected, the values obtained when using a single method show an even greater correlation, as seen in Figures 7c and d. The R^2 value (> 0.999 in all four cases; Fig. 7) confirms the robustness of the estimates from P_{PCA} and $P_{min T}$ methods.

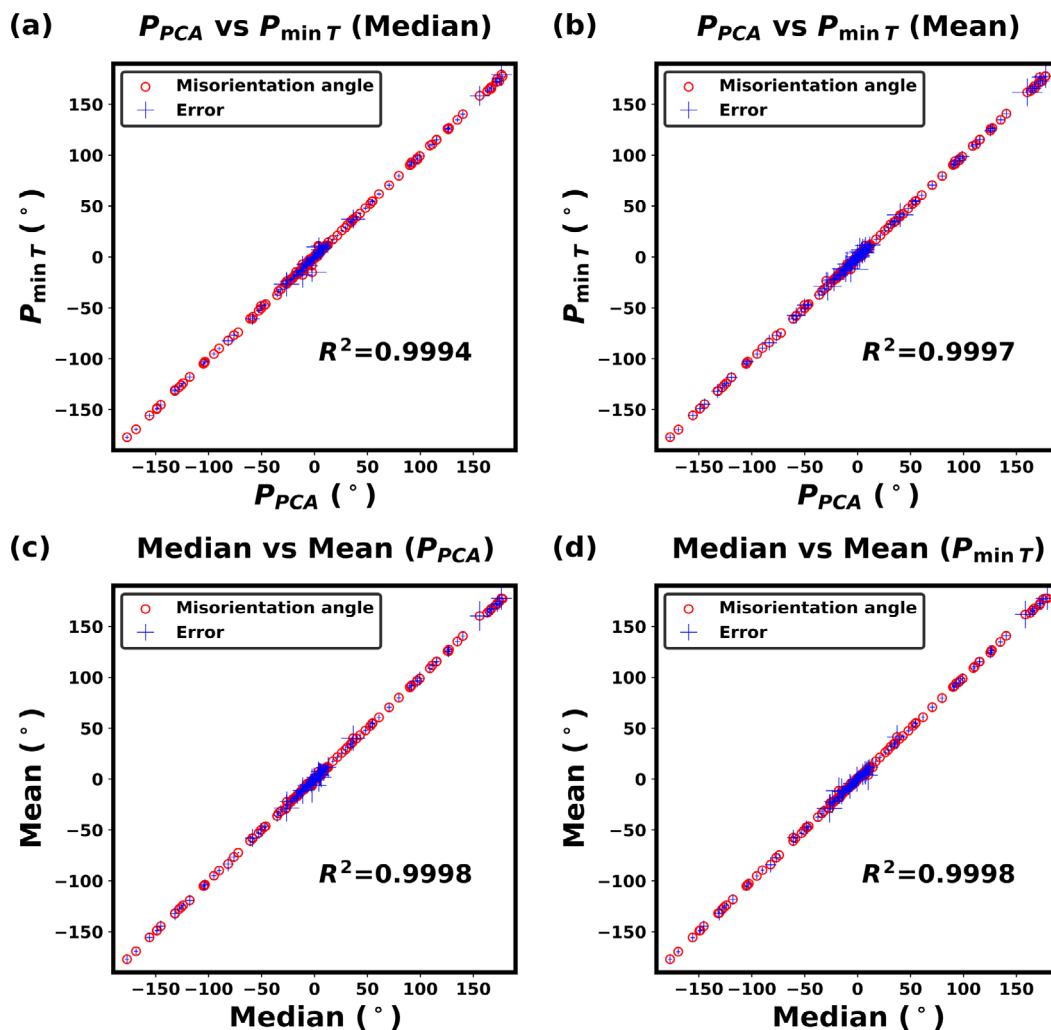


Fig. 7. Median and mean values of misorientation angles calculated from the validation periods of the stations in the KG, KS, and KN networks using P_{PCA} and $P_{min T}$ methods, presented with corresponding MAD and trimmed SD (blue crosses). The R^2 value is presented on the lower right side of each graph, showing strong correlation between values, regardless of the calculation method and the type of representative value used.

4.4. Misorientation of Seismometers in the KG, KS, and KN Network

Since most stations of the KG and KS networks have been in operation for more than 10 years, some of these stations can experience several rotations during the operation period. We obtained 59 and 178 validation periods out of 26 and 111 stations in these networks, respectively. While the majority of stations have not shown any substantial change in horizontal orientation (only 15 and 33 stations in the KG and KS networks, respectively, rotated at least once), some stations have undergone rotation more than three consecutive times. By contrast, stations in the KN network recorded at most 35 earthquakes, given the short operation time. Despite the limited number of events available, all the 13 stations in the KN network have a single validation period with one estimated misorientation angle and the corresponding error within 10° .

The difference in misorientation angle between seismometers is most pronounced when comparing those deployed on the surface with those installed in the borehole. Borehole seismometers can be usually rotated during their deployment and their misorientation angles remain unknown (Ensing and van Wijk, 2018). Figure 8 shows histograms of misorientation angles, each

calculated within a validation period for the surface seismometers and borehole seismometers in the KG, KS, and KN network. It is clear that the number of validation periods is reaching its peak near 0° and decreases steeply as the misorientation angles deviate from 0° in the case of surface seismometers (Fig. 8). However, the dispersion of misorientation angles seems significantly larger for borehole seismometers (Fig. 8). This contrast is prominent regardless of calculation method and type of representative value. Table 2 shows the proportion of validation periods with misorientation in the given range. The proportion with misorientation angle near 0° is smaller for borehole seismometers, whereas the trend is the opposite as it deviates from the geographic north. Figure 9 illustrates the misorientation angles for both surface and borehole stations on 1 March 2020.

We compared the dates for the replacement of sensor or recorder specified in the KIGAM log to the validation periods to check whether each change in the station is related to the change in misorientation angle. We confirmed that 10 stations and 2 stations experienced significant rotation after changing velocimeter and recorder at least once, respectively. We infer that the horizontal sensors would have rotated in the process of being replaced or being connected to a replaced recorder. In addition, we verified the robustness of our estimates through

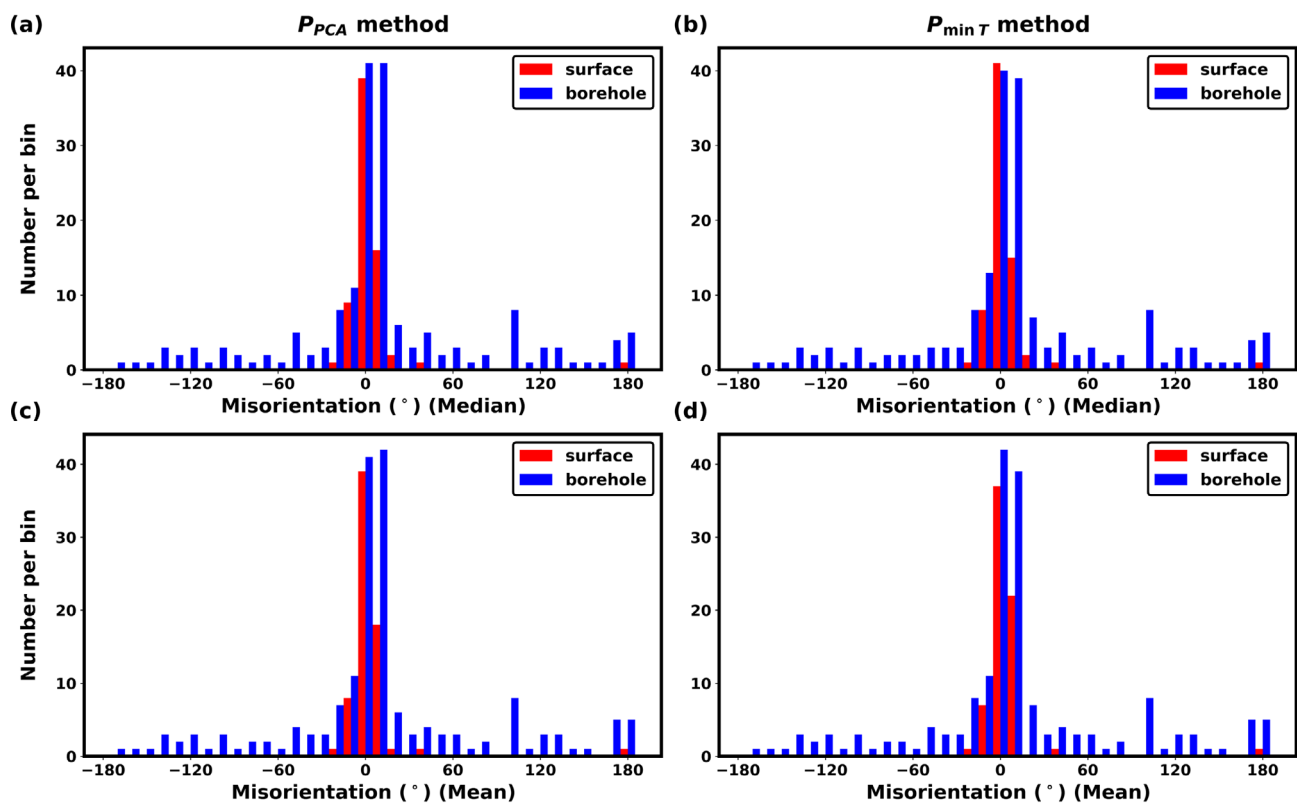


Fig. 8. Histograms showing the distribution of median and mean of misorientation angles calculated within each validation period of stations in the KG, KS, and KN networks using P_{PCA} and $P_{min T}$ methods. The red and blue bars correspond to stations with surface seismometers and borehole seismometers, respectively.

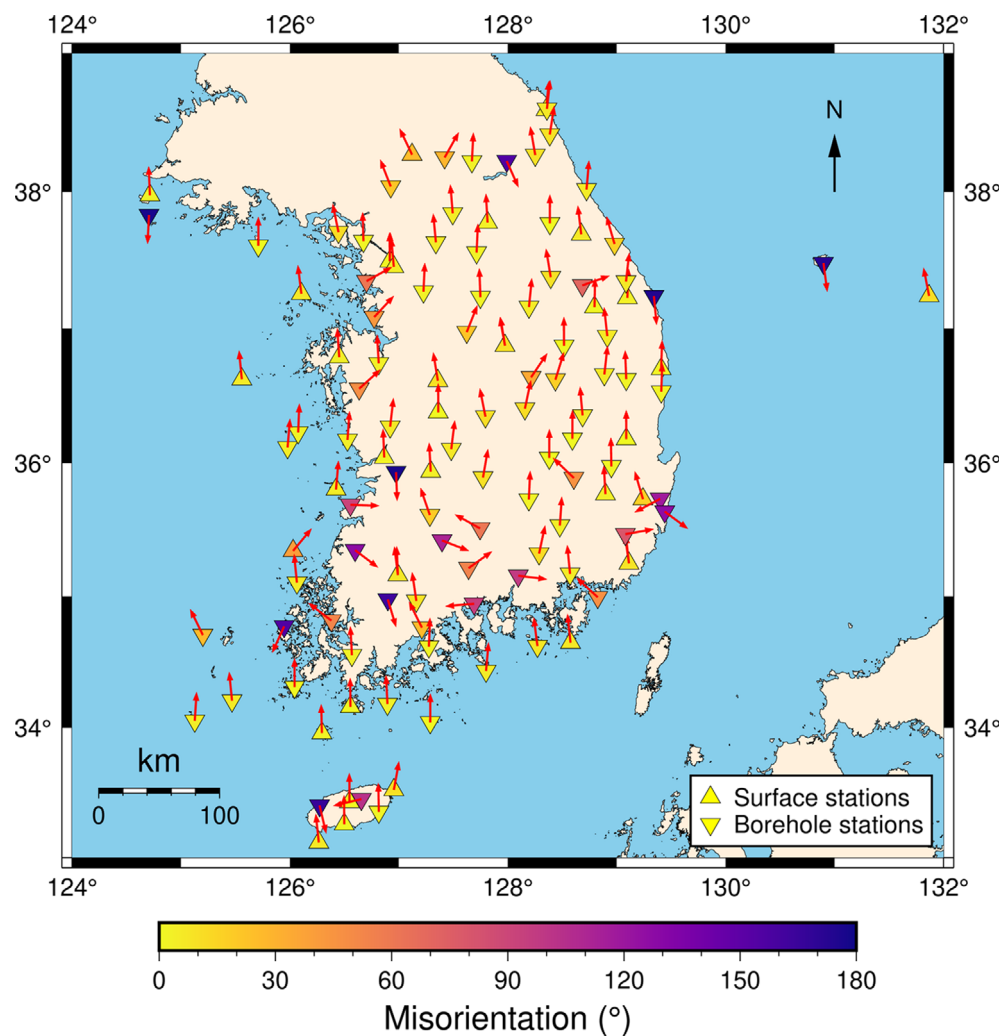


Fig. 9. Map of stations and their corresponding misorientation angles on 1 March 2020. Stations with surface seismometers and borehole seismometers are marked as triangles and inverted triangles, respectively, with each red arrow indicating the direction in which N-S component sensors are aligned. Color of each triangle represents the absolute deviation of N-S sensor from the geographic north, as shown in the color bar below the map.

Table 2. Misorientation angles for seismic stations in the KG, KS, and KN networks

	$\theta_M < 5^\circ$	$\theta_M > 10^\circ$	$\theta_M > 30^\circ$	$\theta_M > 50^\circ$
P_{PCA} (median)	88.41% ^(a)	5.80%	2.90%	1.45%
	66.30%	27.07%	22.10%	18.23%
P_{PCA} (trimmed mean)	91.30%	4.35%	2.90%	1.45%
	65.19%	27.07%	22.10%	18.23%
$P_{min T}$ (median)	91.30%	5.80%	2.90%	1.45%
	64.64%	27.62%	22.10%	18.23%
$P_{min T}$ (trimmed mean)	92.75%	2.90%	2.90%	1.45%
	64.64%	27.62%	22.10%	18.23%

^(a)The percentage of the observations satisfying each criterion is presented for each combination of method and representative value. The upper half and lower half of each cell indicate the proportion of validation periods satisfying given condition for surface seismometers and borehole seismometers, respectively (n = 250).

synthetic waveform calculation. We generated synthetic waveforms of the 21 April 2019 Uljin earthquake (Fig. 1) to compare against the recorded waveforms. For the synthetics, we considered the

solution of strike, dip, and rake of the Uljin earthquake (Fig. 10a; Korea Meteorological Administration, 2019), and used one-dimensional velocity model of the Korean Peninsula (Kim et al.,

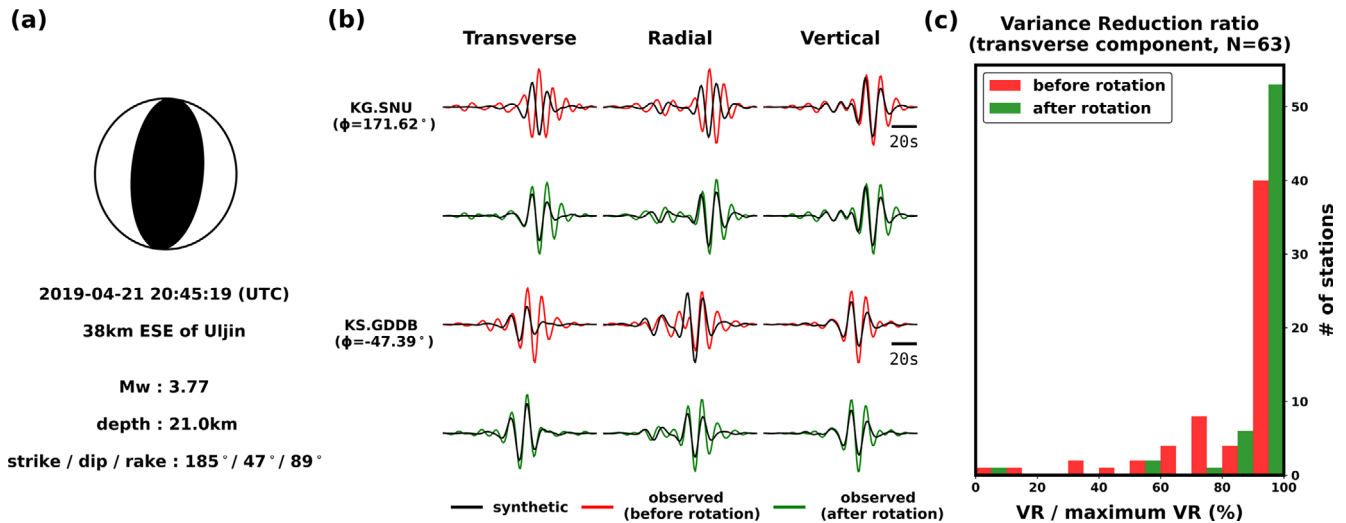


Fig. 10. Comparison of recorded and synthetic waveforms of the 21 April 2019 Uljin earthquake. (a) Beachball plot and source parameters of the Uljin earthquake (Fig. 1, yellow star). (b) Recorded waveforms and synthetic waveforms calculated for stations SNU and GDDB (Fig. 1, yellow triangle and inverted triangle, respectively). Synthetic waveforms are marked as black lines, whereas the recorded waveforms are marked as red lines and green lines before and after rotation of horizontal components, respectively. (c) Histogram of relative VR of transverse component for 63 stations in the KG and KS network. Red bars and green bars indicate the number of stations with corresponding relative VR before and after rotation, respectively.

2011) and wavenumber integration code (Herrmann, 2013) for 63 stations with validation period including the event origin time. We applied zero-phase band-pass filtering within the frequency range of 0.05–0.1 Hz to both recorded and synthetic waveforms. Figure 10b shows examples of the waveforms (one synthetic waveform and two real waveforms before and after rotation for each station) for two stations, where we observe significant improvement in the similarity of radial and transverse components between real and synthetic waveforms after the rotation. To evaluate the improvement quantitatively, we calculated the variance reduction (VR; Scognamiglio et al., 2009) of transverse component between recorded waveform and its synthetic counterpart before and after the rotation, respectively, for all 63 stations using the equation below.

$$VR = \left(1 - \frac{\sum_{i=1}^n |S_i - R_i|^2}{\sum_{i=1}^n R_i^2} \right) \times 100\% . \quad (7)$$

We calculated relative VR, defined as VR with respect to the maximum VR obtained by rotating the horizontal components from 0° to 360° at intervals of 1° . The number of stations with relative VR of transverse component above 90% increased from 40 to 53 after rotation (Fig. 10c).

5. CONCLUSIONS

We estimated the misorientation of 150 broadband seismometers of permanent stations in South Korea by analyzing *P*-wave particle motion via principal component analysis and minimization of

transverse component energy. After defining the length of signal window and the lower bound of SNR and recti *P*/CC, we calculated the misorientation angle from each seismic event and checked if there were significant changes in misorientation angle over time by utilizing the successive procedure of PELT and visual scrutiny. Our estimates are robust, showing R^2 over 0.999 for both median and trimmed mean, with MAD and trimmed SD less than 10° for more than 90% of the entire stations, respectively. More than 80% of surface seismometers are aligned within 10° from the geographic north, whereas over 30% of borehole seismometers experience rotations with angles more than 10° . Furthermore, we find that the timing of the orientation change correlates with the timing of instrument replacement or repair for the KG network. In the electronic supplementary material, we provide a table containing median, trimmed mean, MAD, and trimmed SD for each validation period that researchers can refer to when analyzing waveforms recorded in the corresponding period.

DATA AND RESOURCES

Waveform data of the KS network were retrieved from the National Earthquake Comprehensive Information System (NECIS) website (<http://necis.kma.go.kr>) upon approval, and the data of the KG and KN network are available with the permission of KIGAM and KHNP, respectively. All the data were last accessed in March 2021. We used *ObsPy* (<https://github.com/obspy/obspy/wiki>) for processing the waveform data. Change point detection by PELT was performed using a Python library *ruptures* (<https://github.com/ruptures/ruptures>).

/centre-borelli.github.io/ruptures-docs/). We used *Computer Programs in Seismology (CPS)* (<http://www.eas.slu.edu/eqc/eqccps.html>) and *pyfk* (<https://github.com/ziyixi/pyfk>) for calculating synthetic seismogram.

ACKNOWLEDGMENTS

This work was supported by SNU Student-directed Education Undergraduate Research Program through the Faculty of Liberal Education, Seoul National University (2020). The authors thank W.-Y. Kim, H. Lim, H. Kang, and J.Y. Park in Seoul National University for assistance on data curation and constructive suggestions which improved the quality of the work. The authors acknowledge support from the Nuclear Safety Research Program through the Korea Foundation of Nuclear Safety (KoFONS), granted financial resource from the Nuclear Safety and Security Commission (NSSC), Republic of Korea (No. 1705010). Y. Kim acknowledges support from Creative-Pioneering Researchers Program through Seoul National University (SNU SRnD 3345-20160014).

REFERENCES

- Aminikhanghahi, S. and Cook, D.J., 2017, A survey of methods for time series change point detection. *Knowledge and Information Systems*, 51, 339–367.
- Beyreuther, M., Barsch, R., Krischer, L., Megies, T., Behr, Y., and Wassermann, J., 2010, ObsPy: a Python toolbox for seismology. *Seismological Research Letters*, 81, 530–533.
- Braunmiller, J., Nabelek, J., and Ghods, A., 2020, Sensor orientation of Iranian broadband seismic stations from P-wave particle motion. *Seismological Research Letters*, 91, 1660–1671.
- Büyükkapınar, P., Aktar, M., Maria Petersen, G., and Köseoğlu, A., 2021, Orientations of broadband stations of the KOERI seismic network (Turkey) from two independent methods: P-and Rayleigh-wave polarization. *Seismological Research Letters*, 92, 1512–1521.
- Doran, A.K. and Laske, G., 2017, Ocean-bottom seismometer instrument orientations via automated Rayleigh-wave arrival-angle measurements. *Bulletin of the Seismological Society of America*, 107, 691–708.
- Eisermann, A.S., Ziv, A., and Wust-Bloch, G.H., 2015, Real-time back azimuth for earthquake early warning. *Bulletin of the Seismological Society of America*, 105, 2274–2285.
- Ekström, G. and Busby, R.W., 2008, Measurements of seismometer orientation at USArray transportable array and backbone stations. *Seismological Research Letters*, 79, 554–561.
- Ekström, G. and Nettles, M., 2018, Observations of seismometer calibration and orientation at USArray stations, 2006–2015. *Bulletin of the Seismological Society of America*, 108, 2008–2021.
- Ensing, J.X. and van Wijk, K., 2018, Estimating the orientation of borehole seismometers from ambient seismic noise. *Bulletin of the Seismological Society of America*, 109, 424–432.
- Harris, C.R., Millman, K.J., van der Walt, S.J., Gommers, R., Virtanen, P., Cournapeau, D., and Kern, R., 2020, Array programming with NumPy. *Nature*, 585, 357–362.
- Herrmann, R.B., 2013, Computer programs in seismology: an evolving tool for instruction and research. *Seismological Research Letters*, 84, 1081–1088.
- Jurkevics, A., 1988, Polarization analysis of three-component array data. *Bulletin of the Seismological Society of America*, 78, 1725–1743.
- Kang, T.S. and Baag, C.E., 2004, The 29 May 2004, Mw = 5.1, offshore Uljin earthquake, Korea. *Geosciences Journal*, 8, 115–123.
- Kennett, B.L.N. and Engdahl, E.R., 1991, Traveltimes for global earthquake location and phase identification. *Geophysical Journal International*, 105, 429–465.
- Killick, R., Fearnhead, P., and Eckley, I.A., 2012, Optimal detection of changepoints with a linear computational cost. *Journal of the American Statistical Association*, 107, 1590–1598.
- Kim, K.H., Ree, J.H., Kim, Y., Kim, S., Kang, S.Y., and Seo, W., 2018, Assessing whether the 2017 Mw 5.4 Pohang earthquake in South Korea was an induced event. *Science*, 360, 1007–1009.
- Kim, S., Rhie, J., and Kim, G., 2011, Forward waveform modelling procedure for 1-D crustal velocity structure and its application to the southern Korean Peninsula. *Geophysical Journal International*, 185, 453–468.
- Kim, W.Y., Choi, H., and Noh, M., 2010, The 20 January 2007 Odaesan, Korea, earthquake sequence: reactivation of a buried strike-slip fault? *Bulletin of the Seismological Society of America*, 100, 1120–1137.
- Kim, Y., He, X., Ni, S., Lim, H., and Park, S.C., 2017, Earthquake source mechanism and rupture directivity of the 12 September 2016 Mw 5.5 Gyeongju, South Korea, earthquake. *Bulletin of the Seismological Society of America*, 107, 2525–2531.
- Kim, Y., Rhie, J., Kang, T.S., Kim, K.H., Kim, M., and Lee, S.J., 2016, The 12 September 2016 Gyeongju earthquakes: 1. Observation and remaining questions. *Geosciences Journal*, 20, 747–752.
- Korea Meteorological Administration, 2019, Earthquake Annual Report. Korea Meteorological Administration, Seoul, 220 p. https://www.kma.go.kr/download_01/earthquake/earthquake_2019.pdf [Accessed on 19 September 2021].
- Laske, G., Masters, G., and Zu, W., 1994, Frequency-dependent polarization measurements of long-period surface waves and their implications for global phase-velocity maps. *Physics of the Earth and Planetary Interiors*, 84, 111–137.
- Lee, H. and Sheen, D.H., 2015, A study on determination of orientation of borehole seismometer. *Journal of the Geological Society of Korea*, 51, 93–103.
- Lee, S.J. and Rhie, J., 2015, Determining the orientations of broadband stations in South Korea using ambient noise cross-correlation. *Geophysics and Geophysical Exploration*, 18, 85–90.
- Lim, H., Deng, K., Kim, Y.H., Ree, J.H., Song, T.R., and Kim, K.H., 2020, The 2017 Mw 5.5 Pohang earthquake, South Korea, and poroelastic stress changes associated with fluid injection. *Journal of Geophysical Research: Solid Earth*, 125, e2019JB019134. <https://doi.org/10.1029/2019JB019134>
- Lim, H. and Kim, Y.H., 2020, A dataset of seismic sensor responses of South Korea seismic stations. *Journal of the Geological Society of*

- Korea, 56, 515–524.
- Lim, H., Kim, Y., Song, T.R.A., and Shen, X., 2018, Measurement of seismometer orientation using the tangential *P*-wave receiver function based on harmonic decomposition. *Geophysical Journal International*, 212, 1747–1765.
- Liu, K.H. and Gao, S.S., 2013, Making reliable shear-wave splitting measurements. *Bulletin of the Seismological Society of America*, 103, 2680–2693.
- Niu, F., Bravo, T., Pavlis, G., Vernon, F., Rendon, H., Bezada, M., and Levander, A., 2007, Receiver function study of the crustal structure of the southeastern Caribbean plate boundary and Venezuela. *Journal of Geophysical Research: Solid Earth*, 112, B11308.
- Niu, F. and Li, J., 2011, Component azimuths of the CEArray stations estimated from *P*-wave particle motion. *Earthquake Science*, 24, 3–13.
- Ojo, A.O., Zhao, L., and Wang, X., 2019, Estimations of sensor misorientation for broadband seismic stations in and around Africa. *Seismological Research Letters*, 90, 2188–2204.
- Park, D., Cho, S.I., Lee, Y.H., Choi, W.H., Lee, D.H., and Kim, H.S., 2018, Site monitoring system of earthquake, fault and slope for nuclear power plant sites. *Economic and Environmental Geology*, 51, 185–201.
- Pearson, K., 1901, Principal components analysis. *The London, Edinburgh, and Dublin Philosophical Magazine and Journal of Science*, 6, 559–572.
- Rueda, J. and Mezcuá, J., 2015, Orientation analysis of the Spanish Broadband National Network using Rayleigh-wave polarization. *Seismological Research Letters*, 86, 929–940.
- Scholz, J.R., Barruol, G., Fontaine, F.R., Sigloch, K., Crawford, W., and Deen, M., 2017, Orienting ocean-bottom seismometers from *P*-wave and Rayleigh wave polarisations. *Geophysical Journal International*, 208, 1277–1289.
- Scognamiglio, L., Tinti, E., and Michelini, A., 2009, Real-time determination of seismic moment tensor for the Italian region. *Bulletin of the Seismological Society of America*, 99, 2223–2242.
- Shin, J.S., Sheen, D.H., and Shin, I.C., 2009, Orientation correction for borehole seismic stations in South Korea. *Journal of the Geological Society of Korea*, 45, 47–54.
- Stachnik, J.C., Sheehan, A.F., Zietlow, D.W., Yang, Z., Collins, J., and Ferris, A., 2012, Determination of New Zealand ocean bottom seismometer orientation via Rayleigh-wave polarization. *Seismological Research Letters*, 83, 704–713.
- Truong, C., Oudre, L., and Vayatis, N., 2018, Ruptures: change point detection in Python. *arXiv Preprint*, arXiv:1801.00826.
- Wang, X., Chen, Q.F., Li, J., and Wei, S., 2016, Seismic sensor misorientation measurement using *P*-wave particle motion: an application to the NECsaids Array. *Seismological Research Letters*, 87, 901–911.
- Woo, J.U., Rhie, J., Kim, S., Kang, T.S., Kim, K.H., and Kim, Y., 2019, The 2016 Gyeongju earthquake sequence revisited: aftershock interactions within a complex fault system. *Geophysical Journal International*, 217, 58–74.
- Xu, H., Luo, Y., Tang, C.C., Zhao, K., Xie, J., and Yang, X., 2018, Systemic comparison of seismometer horizontal orientations based on teleseismic earthquakes and ambient-noise data. *Bulletin of the Seismological Society of America*, 108, 3576–3589.
- Xu, W., Yuan, S., Wang, W., Luo, X., and Li, L., 2020, Comparing orientation analysis methods for a shallow-water ocean-bottom seismometer array in the Bohai Sea, China. *Bulletin of the Seismological Society of America*, 110, 3174–3184.
- Zahradník, J. and Custódio, S., 2012, Moment tensor resolvability: application to southwest Iberia. *Bulletin of the Seismological Society of America*, 102, 1235–1254.
- Zeng, S., Zheng, Y., Niu, F., and Ai, S., 2020, Measurements of seismometer orientation of the first phase CHINArray and their implications on vector-recording-based seismic studies. *Bulletin of the Seismological Society of America*, 111, 36–49.
- Zha, Y., Webb, S.C., and Menke, W., 2013, Determining the orientations of ocean bottom seismometers using ambient noise correlation. *Geophysical Research Letters*, 40, 3585–3590.
- Zheng, H., Fan, J., Zhao, D., Li, C., Dong, D., Zhang, G., and Wang, X., 2020, A new method to estimate ocean-bottom-seismometer orientation using teleseismic receiver functions. *Geophysical Journal International*, 221, 893–904.
- Zhu, H., Tian, Y., Zhao, D., Li, H., and Liu, C., 2019, Seismic structure of the Changbai intraplate volcano in NE China from joint inversion of ambient noise and receiver functions. *Journal of Geophysical Research: Solid Earth*, 124, 4984–5002.
- Zhu, G., Yang, H., Lin, J., and You, Q., 2020, Determining the orientation of ocean-bottom seismometers on the seafloor and correcting for polarity flipping via polarization analysis and waveform modeling. *Seismological Research Letters*, 91, 814–825.

Publisher's Note Springer Nature remains neutral with regard to jurisdictional claims in published maps and institutional affiliations.